

# High-Accuracy X-Ray Diffraction Analysis of Phase Evolution Sequence During Devitrification of Cu<sub>50</sub>Zr<sub>50</sub> Metallic Glass

I. KALAY, M.J. KRAMER, and R.E. NAPOLITANO

Real-time high-energy X-ray diffraction (HEXRD) was used to investigate the crystallization kinetics and phase selection sequence for constant-heating-rate devitrification of fully amorphous Cu<sub>50</sub>Zr<sub>50</sub>, using heating rates from 10 K/min to 60 K/min (10 °C/min to 60 °C/min). *In situ* HEXRD patterns were obtained by the constant-rate heating of melt-spun ribbons under synchrotron radiation. High-accuracy phase identification and quantitative assessment of phase fraction evolution through the duration of the observed transformations were performed using a Rietveld refinement method. Results for 10 K/min (10 °C/min) heating show the apparent simultaneous formation of three phases, orthorhombic Cu<sub>10</sub>Zr<sub>7</sub>, tetragonal CuZr<sub>2</sub> (C11<sub>b</sub>), and cubic CuZr (B2), at 706 K (433 °C), followed immediately by the dissolution of the CuZr (B2) phase upon continued heating to 789 K (516 °C). Continued heating results in reprecipitation of the CuZr (B2) phase at 1002 K (729 °C), with the material transforming completely to CuZr (B2) by 1045 K (772 °C). The Cu<sub>5</sub>Zr<sub>8</sub> phase, previously reported to be a devitrification product in Cu<sub>50</sub>Zr<sub>50</sub>, was not observed in the present study.

DOI: 10.1007/s11661-010-0531-9

© The Minerals, Metals & Materials Society and ASM International 2010

## I. INTRODUCTION

ALTHOUGH the investigation of glass formation in metallic systems has uncovered numerous systems with high glass forming ability, leading to the development of several so-called bulk metallic glasses (BMGs) with noteworthy mechanical, electrical, and chemical properties,<sup>[1–4]</sup> the effective application of these materials is somewhat hindered by our limited ability to control the complex phase transition dynamics that result in crystalline structures during solidification of a highly undercooled melt or devitrification of a glassy solid. Moreover, several recently reported examples exist of amorphous-crystalline composite (ACC) materials that illustrate the great potential value of controlled devitrification as a means to obtain novel structures of metastable phases.<sup>[5–7]</sup> In such cases, *in situ* and *ex situ* methods have been investigated with respect to their utility in enabling control of phase selection and composite structure.<sup>[8–10]</sup> Here, we focus on the devitrification behavior in Cu–Zr, a binary system upon which several BMG alloys are based. Of course, reliable prediction and control of phase selection and structural dynamics requires quantification of system thermodynamics as well as an understanding of the kinetic mechanisms involved in solidification/devitrification processes, and advances in the thermodynamics and

structure of Cu–Zr liquids, glasses, and crystalline phases recently have been reported.<sup>[11–13]</sup> Indeed, with numerous stable and metastable crystalline phases, this system offers an immense spectrum of potentially accessible structures and properties and has attracted much attention related to BMGs,<sup>[14–16]</sup> crystallization structures,<sup>[17–19]</sup> and ACC materials.<sup>[20,21]</sup>

A review of prior thermodynamic treatments for the Cu–Zr system was reported recently, and the assessed phase diagram is shown in Figure 1.<sup>[22]</sup> The crystalline phases observed in this system are summarized in Table I. We focus the present investigation on the Cu<sub>50</sub>Zr<sub>50</sub> composition, for which several stable and metastable phases have been observed upon solidification from the melt and devitrification from the glass.<sup>[17–19]</sup> The first systematic study of crystallization from the glass in this alloy was reported by Freed *et al.*,<sup>[46]</sup> who used X-ray diffraction (XRD), differential scanning calorimetry (DSC), and transmission electron microscopy (TEM) to investigate the crystallization of splat quenched glassy alloy, reporting primary crystallization involving an unidentified metastable phase. Using XRD to investigate phase transitions in melt-spun ribbons on heating, Altounian subsequently reported that devitrification occurs in a single reaction from an amorphous phase to a two-phase structure, with Cu<sub>10</sub>Zr<sub>7</sub> being the major phase and CuZr<sub>2</sub> being the minor phase.<sup>[19]</sup> Attempting to resolve this complex transformation path using dynamic temperature X-ray diffraction (DTXRD), Kneller *et al.* reported that the formation of a transient cubic CuZr (B2) phase precedes the formation of the Cu<sub>10</sub>Zr<sub>7</sub> and CuZr<sub>2</sub> phases during continuous heating at a rate of 0.835 K/min (0.835 °C/min).<sup>[17]</sup> They also reported that a Cu<sub>5</sub>Zr<sub>8</sub> phase forms upon heating through an eutectoid invariant temperature of 985 K (712 °C), above which a mixture of Cu<sub>10</sub>Zr<sub>7</sub> and Cu<sub>5</sub>Zr<sub>8</sub>

I. KALAY, Ph.D. Candidate, is with the Department of Materials Science and Engineering, Iowa State University, Ames, IA 50011. M.J. KRAMER, Senior Scientist, is with the Ames Laboratory, U.S. Department of Energy, Ames, IA 50011. R.E. NAPOLITANO, Associate Professor, is with the Department of Materials Science and Engineering, Iowa State University, is also a Scientist with Ames Laboratory, U.S. Department of Energy. Contact e-mail: ralphn@iastate.edu

Manuscript submitted April 12, 2010.

Article published online November 24, 2010

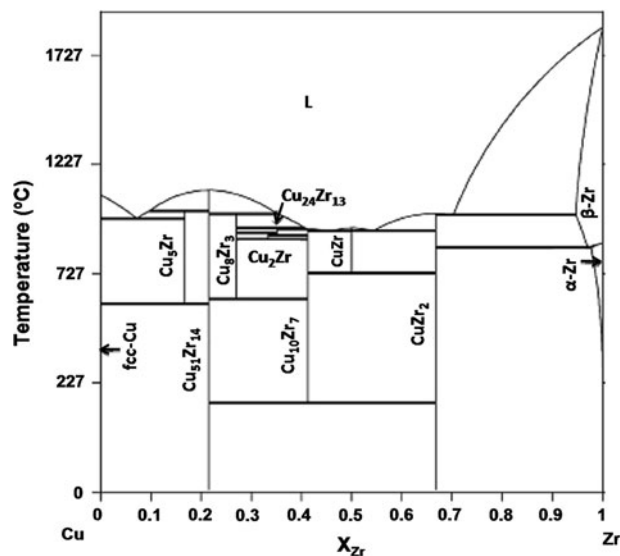


Fig. 1—The equilibrium Cu-Zr Phase Diagram.<sup>[22]</sup>

**Table I. Stable and Metastable (\*) Phases Reported in the Cu-Zr System**

Stoichiometry	Prototype	Structural Designation	Space Group	Ref.
Cu	Cu	A1	Fm $\bar{3}$ m	[23]
Cu <sub>5</sub> Zr	AuBe <sub>5</sub>		F43m	[24–27]
Cu <sub>9</sub> Zr <sub>2</sub>				[28]
Cu <sub>51</sub> Zr <sub>14</sub>	Ag <sub>51</sub> Gd <sub>14</sub>		P6/m	[29,30]
Cu <sub>7</sub> Zr <sub>2</sub> *			C2/m	[31]
Cu <sub>3</sub> Zr*			P6 <sub>3</sub> /mmc	[32]
Cu <sub>8</sub> Zr <sub>3</sub>	Cu <sub>8</sub> Hf <sub>3</sub>		Pnma	[29,33]
Cu <sub>2</sub> Zr			Fd $\bar{3}$ m	[34]
Cu <sub>24</sub> Zr <sub>13</sub>				[35]
Cu <sub>10</sub> Zr <sub>7</sub>	Ni <sub>10</sub> Zr <sub>7</sub>		Aba2	[27,29]
Cu <sub>10</sub> Zr <sub>7</sub>			Cmca	[36]
Cu <sub>10</sub> Zr <sub>7</sub>			Pbca	[37]
Cu <sub>11</sub> Zr <sub>9</sub>			I4/m	[38]
CuZr	CsCl	B2	Pm $\bar{3}$ m	[39]
CuZr*		B19'	P2 <sub>1</sub> /m	[40]
CuZr*		B33	Cmcm	[41]
CuZr*	$\gamma$ -CuTi	B11	P4/nmm	[42]
CuZr*	AuCu-I	L1 <sub>0</sub>	P4/mmm	[42]
CuZr*	$\beta$ -AuCd	B19	Pmma	[42]
Cu <sub>5</sub> Zr <sub>8</sub>			R3m	[43]
Cu <sub>5</sub> Zr <sub>8</sub>			I43m	[44]
Cu <sub>5</sub> Zr <sub>8</sub>				[35]
$\beta$ CuZr <sub>2</sub>	MoSi <sub>2</sub>	C11 <sub>b</sub>	I4/mmm	[45]
$\beta$ Zr	W	A2	Im $\bar{3}$ m	[42]
$\alpha$ Zr*	Mg	A3	P6 <sub>3</sub> /mmc	[43]

is observed until the completion of the transition to the CuZr (B2) phase, which is stable from 1003 K (730 °C) to its melting temperature. Although this intermediate temperature range of stability for the Cu<sub>5</sub>Zr<sub>8</sub> phase is consistent with the phase diagram reported by Okamoto,<sup>[47]</sup> it does not agree with the findings of Zhou and Napolitano,<sup>[22]</sup> and additional work may be needed to clarify this issue. In addition to the stable phases that may play a role in the devitrification response of the Cu<sub>50</sub>Zr<sub>50</sub> alloy, it should be noted that

several metastable CuZr phases have been observed. For example, the CuZr (B2) phase has been shown to undergo a martensitic transition to a two-phase structure, reported to consist of a B19' phase<sup>[40]</sup> and a B33 phase.<sup>[48]</sup> Whether such phases play any role in devitrification response and, if so, under what conditions, remains unclear at this time.

In the work presented here, *in situ* high-energy X-ray diffraction (HEXRD) is employed to investigate phase selection and devitrification kinetics in an amorphous Cu<sub>50</sub>Zr<sub>50</sub> alloy, examining specifically the competition of phases observed under constant heating rate conditions. Although a systematic set of isothermal treatments at various temperatures, with time resolved phase identification, is called for to facilitate complete quantification of the devitrification kinetics, we leave that for a later analysis and employ here constant heating rate experiments to resolve the uncertain crystallization sequence, as reported in prior investigations.<sup>[17,19,46]</sup> Accordingly, all diffraction data are analyzed using a Rietveld refinement technique,<sup>[49,50]</sup> providing reliable phase identification and high-accuracy quantification of phase fractions. Herein lies the principal difference between the present work and the prior reports, which rely only on the indexing of the XRD patterns by fitting the interplanar spacings. By incorporating lattice parameters, atomic coordinates, atomic site occupancies, phase fractions, and isotropic thermal displacement parameters into a model of the overall diffraction pattern, the Rietveld refinement method used here provides a means for deconvolution and interpretation of the many overlapping peaks, enabling a reliable quantitative analysis of XRD patterns obtained from multiphase structures observed throughout the course of the devitrification process.

## II. EXPERIMENTAL METHODS

Alloy specimens were prepared from high-purity constituents (0.9999 Cu and 0.9993 Zr, by weight) by arc melting under an argon atmosphere and were remelted and chill-quenched three times for chemical homogeneity. Amorphous alloys were produced from the liquid by free-jet melt spinning<sup>[51,52]</sup> on a copper wheel, at a tangential velocity of 25 m/s, under 0.33 atm He, using a graphite crucible, yielding ribbons that were nominally 1-mm wide and 38- $\mu$ m thick. Each XRD specimen was prepared by cutting the melt-spun ribbons into 12-mm lengths, stacking 40 lengths together, placing the stack into a 2-mm diameter thin-walled quartz capillary tube, and sealing under an Ar atmosphere.

The amorphous nature of the as-quenched Cu<sub>50</sub>Zr<sub>50</sub> specimens was verified using DSC, HEXRD, and TEM. Each DSC specimen (8.00 mg) was sealed in an aluminum pan and placed in a platinum sample holder. DSC scans were performed using a constant heating rate of 10 K/min (10 °C/min), 20 K/min (20 °C/min), 30 K/min (30 °C/min), 40 K/min (40 °C/min), 50 K/min (50 °C/min) and 60 K/min (60 °C/min/min), from room temperature to 843 K (570 °C/min), with temperature and power input accuracies of  $\pm 0.1$  K ( $\pm 0.1$  °C) and

0.2  $\mu$ W, respectively. For each specimen analyzed, multiple scans were performed, and the second scan was taken as an instrument baseline.

*In situ* HEXRD was used to investigate the devitrification process during constant-rate (10 K/min [10 °C/min]) heating. Synchrotron X-rays of 99.586 keV ( $\lambda = 0.0124(5)$  nm) were employed, and diffraction patterns were collected in Deby–Scherrer geometry using a charge-coupled device with an exposure time of 15 seconds and a temperature range between 423 K and 1264 K (150 °C and 991 °C). Diffraction data were analyzed using a Rietveld refinement (fitting) scheme, where the approach is to minimize the function,

$$M = \sum_i^n w_i [I_i^E(Q) - I_i^M(Q, \phi)]^2, \quad [1]$$

which quantifies the integral difference between the experimentally measured diffracted intensity  $I_i^E(Q)$  and a model intensity function  $I_i^M(Q, \phi)$ , where  $w_i$  is a weighting factor,  $Q$  is defined as  $4\pi \sin \theta / \lambda$ ,  $\phi$  represents a set of model parameters that are optimized in the fitting process, and the sum is taken over all ( $n$ ) measured points along  $Q$ . The adjustable and nonadjustable

parameters included in this model are defined in Table II, and the details of the refinement scheme are given the appendix.

III. RESULTS

The HEXRD pattern for the as-quenched ribbon is shown in Figure 2(a), where the broad diffuse scattering peaks indicate that the structure is amorphous. This also is supported by the featureless bright-field TEM image in Figure 2(b) as well as by the corresponding selected area electron diffraction (SAED) pattern in Figure 2(c), showing only broad halo rings. The continuous heating DSC traces for the Cu<sub>50</sub>Zr<sub>50</sub> as-quenched ribbon at 10 K/min (10 °C), 20 K/min (20 °C), 30 K/min (30 °C), 40 K/min (40 °C), 50 K/min (50 °C), and 60 K/min (60 °C/min) are shown in Figure 2(d), each revealing a distinct glass transition feature and exothermic peaks associated with crystallization. The expanded scale inset shows the DSC trace for 10 K/min (10 °C/min), clearly exhibiting (1) the glass transition ( $T_g$ ) at 668 K (395 °C), (2) the onset of crystallization ( $T_x$ ) at 703 K (430 °C),

Table II. Summary of Model Intensity Parameters for Reitveld Refinement

Parameters	Symbol	Equation
Lorentz-polarization factor	$L(\lambda, \theta)$	$L(\lambda, \theta) = \frac{P_h(\lambda) + (1 - P_h(\lambda)) \cos^2 2\theta}{2 \sin^2 \theta \cos \theta}$
Pseudo-Voigt shape function	$PV_p(\theta)$	$PV_p(\theta) = \eta L(\theta) + (1 - \eta) G(\theta)$
Structure factor	$F_p(\theta)$	$ F_p(\theta) ^2 = \left  \sum_p f_p(\theta) e^{2\pi i (k \cdot \vec{r}_n)} \right ^2$
Polarization fraction	$P_h(\lambda)$	
Background intensity	$I_b(\theta)$	$I_b(\theta) = B_1 + \sum_{j=1}^N \left( B_{2j} \frac{(4\pi \sin \theta / \lambda)^{2j}}{j!} + B_{2j+1} \frac{j!}{(4\pi \sin \theta / \lambda)^{2j}} \right)$
Preferred orientation	$P_p$	$P_p = \frac{1}{N} \sum_{i=1}^N [1 + (\tau^2 - 1) \cos^2 \varphi]^{-1/2*}$
Absorption	$A(\lambda)$	$\left( A = \frac{1}{V} \int_V \exp(-\mu_{\text{eff}} l) dV \right)^\dagger$
Phase fraction weighting factor	$s_p$	
Multiplicity	$m_p(\theta)$	

\*The sum is taken over a systematically equivalent reciprocal lattice points and  $\tau$  is the preferred orientation parameter.  
†In the equation,  $V$  is volume of the sample,  $l$  is the total path of both incident and diffracted beam through the sample,  $\mu_{\text{eff}}$  is an effective linear absorption coefficient.  
See appendix for details.

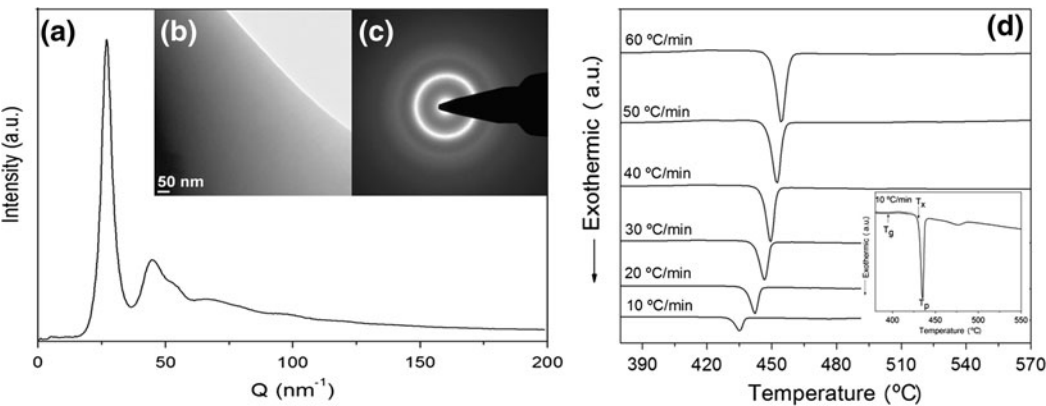


Fig. 2—(a) HEXRD diffraction pattern, (b) BF image with (c) corresponding SAED and (d) isochronal DSC plots at 10 K/min (10 °C/min), 20 K/min (20 °C/min), 30 K/min (30 °C/min), 40 K/min (40 °C/min), 50 K/min (50 °C/min), and 60 K/min (60 °C/min) with inset shows the DSC trace at 10 K/min (10 °C/min) of the as-quenched Cu<sub>50</sub>Zr<sub>50</sub> ribbons.

and (3) the temperature of maximum (peak) crystallization rate ( $T_p$ ) 708 K (435 °C). In addition, the thermograph shows a second broad exothermic peak with an onset of 738 K (465 °C).

All three of these characteristic temperatures ( $T_g$ ,  $T_x$ , and  $T_p$ ) were clearly identifiable for all heating rates and each increased with the heating rate, as shown in Figure 3. As a means for considering the mechanisms involved in the crystallization process, we apply a Kissinger analysis<sup>[53]</sup> to model the rate-dependent crystallization temperature ( $T_x$ ) as follows:

$$\ln \phi / T_x^2 = -\frac{E}{RT_x} + \text{const.} \quad [2]$$

where  $\phi$  is the heating rate,  $R$  is the gas constant, and  $E$  is an apparent *net* activation energy associated with all mechanisms that contribute to the observed crystallization process. Based on our DSC results, this is evaluated as 383 kJ/mol, in reasonable agreement with the analyses of Buschow<sup>[18]</sup> and Eifert,<sup>[54]</sup> who reported values of 396 and 396.6 kJ/mol, respectively.

The time-resolved HEXRD data are shown in Figure 4 for heating amorphous CuZr from 423 K (150 °C) to 1264 K (991 °C) at a rate of 10 K/min

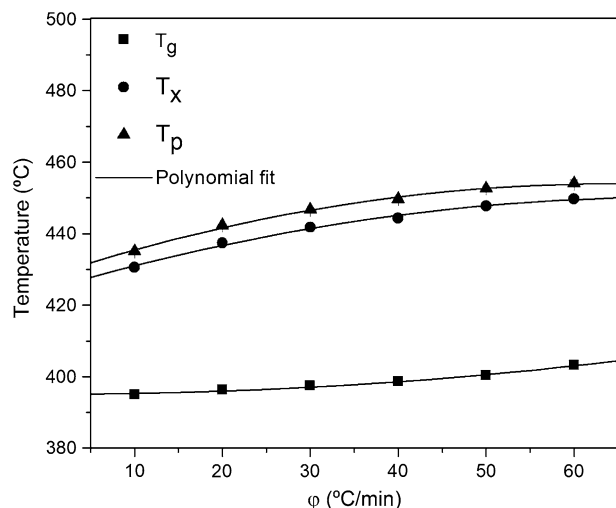


Fig. 3—Characteristic temperatures determined for melt spun  $\text{Cu}_{50}\text{Zr}_{50}$  from DSC traces at different heating rates ( $\phi$ ).

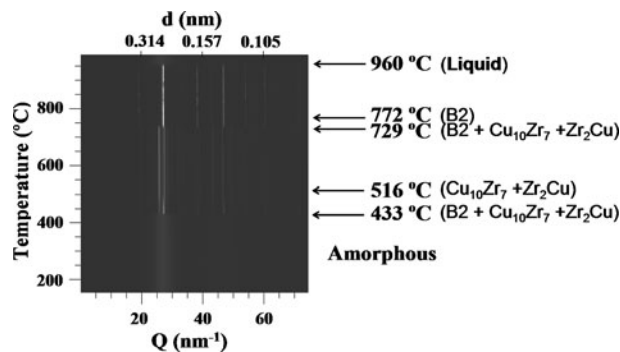


Fig. 4—Two-dimensional representations of diffraction pattern of amorphous  $\text{Cu}_{50}\text{Zr}_{50}$  alloy during devitrification at 10 K/min (10 °C/min).

(10 °C/min). Based on the indicated transitions, we identify several temperature regimes to examine more closely using a quantitative Rietveld refinement scheme, and refined HEXRD patterns are shown in Figure 5 for

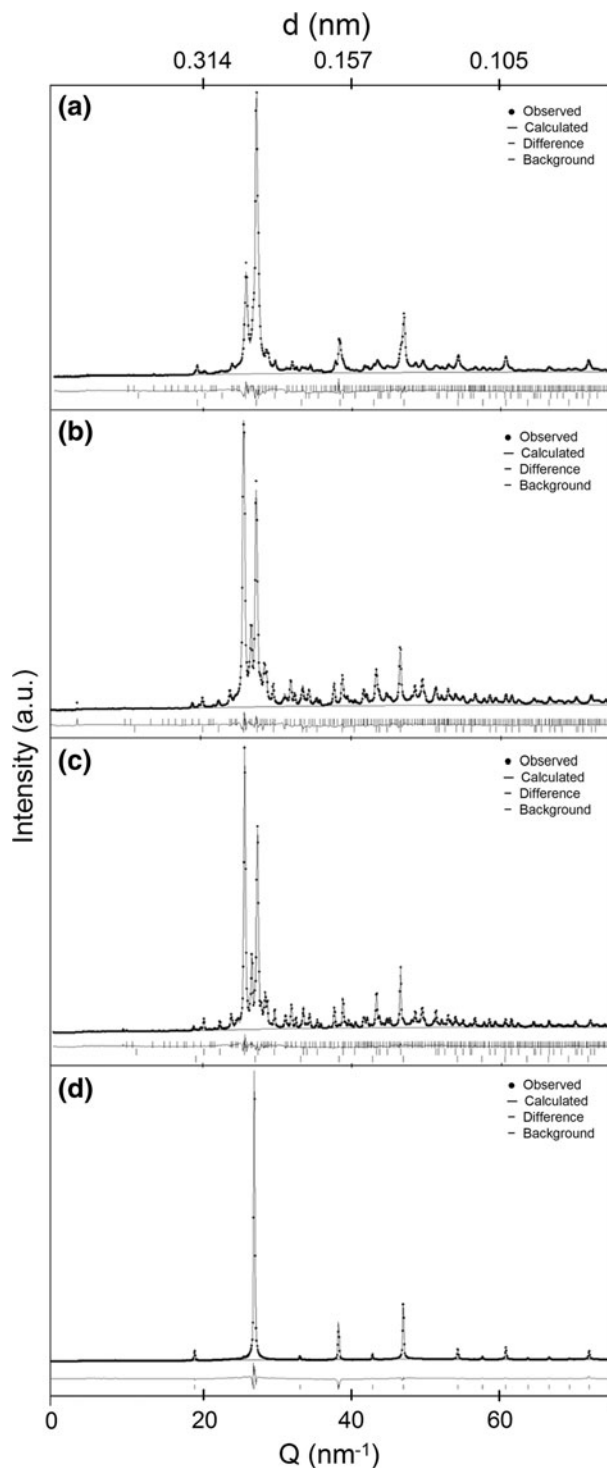


Fig. 5—Rietveld refined diffraction patterns for the data collected at (a) 706 K (433 °C), (b) 789 K (516 °C), (c) 1002 K (729 °C), and (d) 1045 K (772 °C). The vertical marks indicate the reflections for the  $\text{Cu}_{10}\text{Zr}_7$ ,  $\text{CuZr}_2$  and  $\text{CuZr}$  (B2) phases below the XRD plots in (a) and (c), for the  $\text{Cu}_{10}\text{Zr}_7$  and  $\text{CuZr}_2$  phases below the XRD plot in (b), and B2 phase below the XRD plot in (d) from top to bottom, respectively.



**Table III. Fitted Model Parameters During Rietveld Refinement**

Profile Parameters	706 K (433 °C)	789 K (516 °C)	1002 K (729 °C)	1045 K (772 °C)
Phase Scale Factor				
Cu <sub>10</sub> Zr <sub>7</sub>	0.00153	0.00243	0.00250	—
CuZr <sub>2</sub>	0.0088	0.0144	0.0144	—
CuZr (B2)	0.0478	—	0.0018	0.150
Background Coefficients				
B1	0.4065E+02	0.4066E+02	0.3930E+02	0.3599E+02
B2	0.9389E+01	0.8750E+01	0.1121E+02	0.1746E+02
B3	-0.1643E-01	-0.1378E-01	-0.1792E-01	-0.9859E-02
B4	-0.8928E+00	-0.8310E+00	-0.9286E+00	-0.1628E+01
B5	0.1207E-05	0.1103E-05	0.1372E-05	0.7277E-06
B6	0.5815E-01	0.544E-01	0.5217E-01	0.9526E-01
B7	-0.5891E-11	-0.5437E-11	-0.6727E-11	-0.3555E-11
B8	-0.1818E-02	-0.1712E-02	-0.1454E-02	-0.2647E-02
Profile Functions				
Cu <sub>10</sub> Zr <sub>7</sub>				
GW	0.4706E-01	0.2068E+00	0.1551E+00	—
LX	0.2474E+01	0.1667E+01	0.1705E+01	
LY	0.3886E+02	0.2996E+02	0.8943E+01	
CuZr <sub>2</sub>				
GW	0.3247E-01	0.1310E+00	0.2090E+00	—
LX	0.5753E+01	0.1901E+01	0.1700E+01	
LY	0.2766E+02	0.3607E+02	0.1417E+00	
CuZr (B2)				
GW	0.6489E+00	—	0.2110E+00	0.2273E+00
LX	0.7521E+00		0.7330E+00	0.1364E+01
LY	0.6568E+02		0.2891E+02	0.4896E+01

temperatures of 706 (433 °C), 789 (516 °C), 1002 (729 °C) and 1045 K (772 °C). Corresponding fitted model parameters and the refined structural data for each phase are listed in Tables III and IV, respectively.

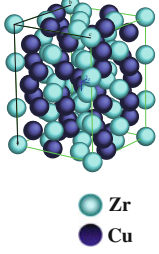

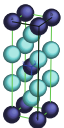
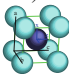
This quantitative analysis facilitates more complete and reliable interpretation of the experimental data. First, the optimized pattern for 706 K (433 °C), in Figure 5(a), confirms that the amorphous Cu<sub>50</sub>Zr<sub>50</sub> initially devitrifies into three phases—Cu<sub>10</sub>Zr<sub>7</sub>, CuZr<sub>2</sub>, and CuZr (B2). We note here that the CuZr (B2) phase is metastable at this temperature and only stable from 1002 K (729 °C) to its melting temperature.<sup>[22]</sup> Figure 5(b) shows the fitted pattern at 789 K (516 °C), where the sharper peaks for the Cu<sub>10</sub>Zr<sub>7</sub> and CuZr<sub>2</sub> phases indicate that the increase in phase fraction is accompanied by an increase in crystallite size. This pattern also shows that the CuZr (B2) phase dissolution is completed at approximately 789 K (516 °C) for this heating rate. Additionally, we note that only the Cu<sub>10</sub>Zr<sub>7</sub> and CuZr<sub>2</sub> phases are present, with no evidence to suggest that the Cu<sub>5</sub>Zr<sub>8</sub> phase appeared at any subsequent time. Figure 5(c) shows the fitted pattern for 1002 K (729 °C), and the appearance of weak peaks for the CuZr (B2) phase supports our preliminary observation that the CuZr (B2) phase forms in this temperature range, where it becomes stable. After the precipitation of the CuZr (B2) phase, the three phases (Cu<sub>10</sub>Zr<sub>7</sub>, CuZr<sub>2</sub>, and CuZr [B2]) coexist until the transformation is complete, with the phase fraction of the CuZr (B2) phase increasing to unity at 1045 K (772 °C), as shown in Figure 5(d). The alloy then melts congruently at 1233 K (960 °C).

## IV. DISCUSSION

Based on our experimental findings, the constant-heating-rate devitrification sequence is summarized in the following list and in Figure 6 (with specific temperatures associated with a heating rate of 10 K/min [10 °C/min]):

- The onset of crystallization ( $T_x = 706$  K [433 °C]) involves the simultaneous (within the limits of temporal resolution) formation of three phases, including Cu<sub>10</sub>Zr<sub>7</sub>, CuZr<sub>2</sub>, and CuZr (B2). This initial crystallization event occurred within a 15-second interval, too rapid to differentiate and resolve the rates of formation associated with the individual phases. After the initial event, the material was completely crystalline with phase fractions of 0.399, 0.223, and 0.378 (by weight) for Cu<sub>10</sub>Zr<sub>7</sub>, CuZr<sub>2</sub>, and CuZr (B2), respectively.
- The initial rapid crystallization event is followed immediately by a slower transition process over the range from 706 K to 789 K (433 °C to 516 °C), characterized by a gradual increase in the fractions of Cu<sub>10</sub>Zr<sub>7</sub> and CuZr<sub>2</sub>, coupled with the simultaneous complete decomposition of the CuZr (B2) phase. At the end of this period, the phase fractions are 0.636 and 0.364 (by weight) for Cu<sub>10</sub>Zr<sub>7</sub> and CuZr<sub>2</sub>, respectively.
- Upon continued heating from 789 K (516 °C) to 1002 K (729 °C), the Cu<sub>10</sub>Zr<sub>7</sub> and CuZr<sub>2</sub> phases remain in equilibrium with no observable changes in phase fractions.
- At 1002 K (729 °C), the reprecipitation of the CuZr (B2) phase is observed. On continued

Table IV. Structural Parameters Refined During Rietveld Modeling

Structure Parameters		706 K (433 °C)	789 K (516 °C)	1002 K (729 °C)	1045 K (772 °C)
 <p><math>\text{Cu}_{10}\text{Zr}_7</math></p> <p></p>	Lattice parameters				
	<i>a</i>	12.714*	12.717	12.7249	—
	<i>b</i>	9.415	9.411	9.442	—
	<i>c</i>	9.414	9.415	9.450	—
	Atomic sites				
	Atom Wyckoff	<i>x, y, z</i>	<i>x, y, z</i>	<i>x, y, z</i>	<i>x, y, z</i>
	Cu 16 g	0.144, 0.020, 0.209	0.144, 0.018, 0.201	0.143, 0.024, 0.210	—
	Cu 16 g	0.358, 0.294, 0.008	0.358, 0.287, 0.009	0.357, 0.295, 0.010	—
	Zr 8 f	0.000, 0.105, 0.390	0.000, 0.106, 0.393	0.000, 0.103, 0.398	—
	Zr 8f	0.000, 0.309, 0.200	0.000, 0.309, 0.200	0.000, 0.309, 0.199	—
	Zr 8e	0.250, 0.264, 0.250	0.250, 0.264, 0.250	0.250, 0.269, 0.250	—
	Zr 8d	0.3074, 0.000, 0.000	0.3076, 0.000, 0.000	0.3076, 0.000, 0.000	—
	Zr 4a	0.000, 0.000, 0.000	0.000, 0.000, 0.000	0.000, 0.000, 0.000	—
	Uiso				
	Cu 16 g	0.010	0.012	0.038	—
	Cu 16 g	0.013	0.021	0.022	—
	Zr 8 f	0.031	0.035	0.035	—
	Zr 8f	0.031	0.027	0.028	—
	Zr 8e	0.013	0.015	0.029	—
	Zr 8d	0.024	0.021	0.028	—
	Zr 4a	0.028	0.026	0.046	—
 <p><math>\text{CuZr}_2</math></p>	Lattice parameters				
	<i>a, b</i>	3.2426	3.2354	3.2419	—
	<i>c</i>	11.163	11.231	11.2651	—
	Atomic sites				
	Atom Wyckoff	<i>x, y, z</i>	<i>x, y, z</i>	<i>x, y, z</i>	<i>x, y, z</i>
	Cu 2a	0.000, 0.000, 0.000	0.000, 0.000, 0.000	0.000, 0.000, 0.000	—
	Zr 4e	0.000, 0.000, 0.3467	0.000, 0.000, 0.3463	0.000, 0.000, 0.3464	—
	Uiso				
	Cu 2a	0.029	0.029	0.047	—
	Zr 4e	0.018	0.017	0.029	—
 <p><math>\text{CuZr}</math> (B2)</p>	Lattice parameters				
	<i>a, b, c</i>	3.2778	—	3.2880	3.28952
	Atomic sites				
	Atom Wyckoff	<i>x, y, z</i>	<i>x, y, z</i>	<i>x, y, z</i>	<i>x, y, z</i>
	Cu 1b	0.500, 0.500, 0.500	—	0.500, 0.500, 0.500	0.500, 0.500, 0.500
	Zr 1a	0.000, 0.000, 0.000	—	0.000, 0.000, 0.000	0.000, 0.000, 0.000
	Uiso				
	Cu 1b	0.036	—	0.01 <sup>†</sup>	0.062
	Zr 1a	0.021	—	0.02 <sup>†</sup>	0.047

\*Underlining is used to indicate the inconsistent digit in the number.

<sup>†</sup>The volume fraction of B2 phase is too small to detect the accurate thermal motion parameter.

heating, the growth of this phase is accompanied by the dissolution of both  $\text{Cu}_{10}\text{Zr}_7$  and  $\text{CuZr}_2$  until the fraction of  $\text{CuZr}$  (B2) reaches unity at 1045 K (772 °C).

- (e) The  $\text{CuZr}$  (B2) melts congruently at 1233 K (960 °C).

Experimental limitations in regard to temporal resolution in the collection of HEXRD patterns do not permit deconvolution of the initial complex crystallization event, involving the formation of three phases. However, Rietveld analysis of the HEXRD patterns does allow reliable determination of the resulting crystallized phase fractions, as listed in item (1) previously. Coupled eutectic-type growth of a three-phase structure is not expected in the binary system, even under these far-from-equilibrium conditions. However, it is likely that some catalytic effect is present between

the phases that promotes rapid nucleation and growth after the initiation of a single phase. As stated previously, detailed elucidation of these nanoscale structural and chemical interactions are beyond the scope of the present study. Focusing on the devitrification sequence, we note that, although the initial crystallization event remains unresolved from a temporal perspective, our *in situ* HEXRD studies, coupled with quantitative Rietveld analysis, permit reliable deconvolution of the secondary phase transformations that follow the primary crystallization process. Indeed, the growth of the  $\text{Cu}_{10}\text{Zr}_7$  and  $\text{CuZr}_2$  phases and the simultaneous dissolution of the  $\text{CuZr}$  (B2) phase were well resolved in time, for the heating rate of 10 K/min (10 °C/min), as shown in Figure 6(a). Moreover, analysis of the DSC traces obtained for heating rates from 10 K/min to 60 K/min (10 °C/min to 60 °C/min) indicate that, although the

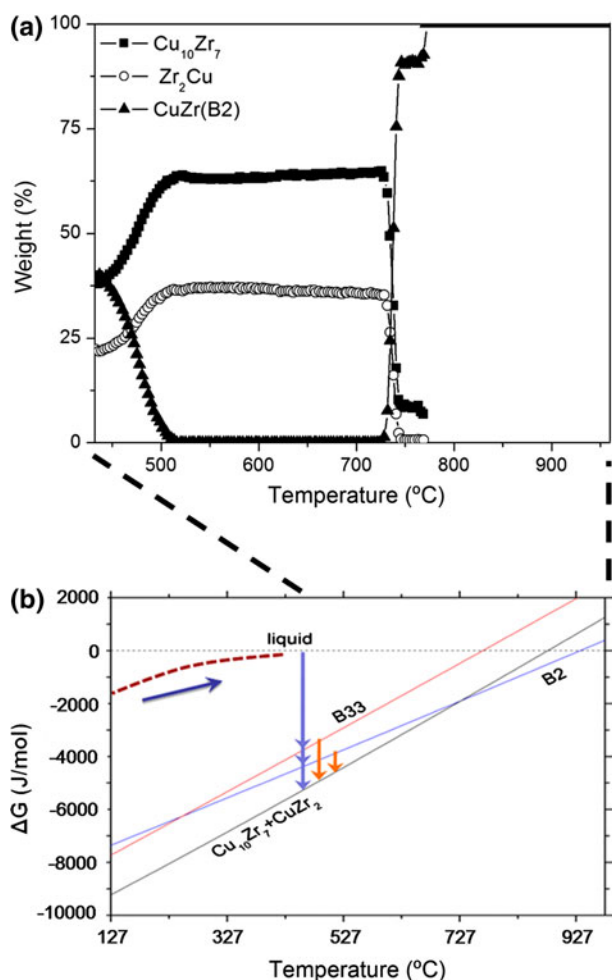


Fig. 6—(a) Weight fractions of  $\text{Cu}_{10}\text{Zr}_7$ ,  $\text{CuZr}_2$  and  $\text{CuZr}$  (B2) phases during continuous heating of  $\text{Cu}_{50}\text{Zr}_{50}$  alloy at 10 K/min (10 °C/min). (b) Free energy curves of metastable and stable phases in  $\text{Cu}_{50}\text{Zr}_{50}$  system in the same temperature range.<sup>[22]</sup>

characteristic temperatures exhibit a shift with heating rate, the transformation seems to remain isokinetic over this range, with a well-defined net activation energy, suggesting that a common set of crystallization mechanisms are operative over this range. Accordingly, although the specific temperatures are influenced by heating rate, the HEXRD data collected at 10 K/min (10 °C/min) can be considered representative of all rates in this range from a mechanistic standpoint.

The sequence of metastable and stable phase formation, indicated by the DSC and HEXRD results, is consistent with the recently reported thermodynamic description of the  $\text{CuZr}$  system,<sup>[22]</sup> as described in Figure 6(b), where the Gibbs free energies of  $\text{CuZr}$  (B2),  $\text{CuZr}$  (B33), and the two-phase  $\text{Cu}_{10}\text{Zr}_7 + \text{CuZr}_2$  mixture, are plotted as a function of temperature for the  $\text{Cu}_{50}\text{Zr}_{50}$  composition. All free energies are given with respect to the liquid free energy, and the free energy of the glass is shown schematically to illustrate the devitrification sequence. It is clear that the driving force for all crystallization processes becomes rather large upon heating above  $T_x$  and  $T_g$ . The decomposition reaction producing  $\text{Cu}_{10}\text{Zr}_7 + \text{CuZr}_2$  is the most strongly driven,

but this process requires chemical partitioning and diffusion and is sluggish. The process with the second highest driving force is the partitionless transition to the  $\text{CuZr}$  (B2) phase, requiring only short-range atomic rearrangements. It is likely therefore that the nucleation of the  $\text{CuZr}$  (B2) phase initiates the crystallization response, but that chemical, interfacial, and volume effects associated with the formation of the  $\text{CuZr}$  (B2) phase quickly reduce the kinetic barriers that inhibit the highly driven formation of the stable  $\text{Cu}_{10}\text{Zr}_7$  and  $\text{CuZr}_2$  phases.

We now raise and briefly discuss three specific points. First, we assert that the structural similarity between  $\text{CuZr}_2$  and  $\text{CuZr}$  (B2) provides an avenue for epitaxial-type transitions from one phase to the other during growth from the glass. This type of devitrification response has been suggested by previously reported experiments involving this system<sup>[17,46]</sup> and other related alloys, such as  $\text{Cu-Zr-Ti}$ <sup>[55]</sup> and  $\text{Cu-Zr-Ti-Pd}$ .<sup>[56]</sup> Some of these observations involve “quenched in” nuclei, but we report that no such crystallites were observed in the melt-spun alloys investigated presently. Second, the structural similarity between the two phases also would serve to reduce the barrier to the reprecipitation of the  $\text{CuZr}$  (B2) phase from the  $\text{Cu}_{10}\text{Zr}_7 + \text{CuZr}_2$  two-phase structure, observed upon heating above 1002 K (729 °C), where this phase becomes stable (Figure 5). Third, although Kneller *et al.* reported<sup>[17]</sup> the formation of  $\text{Cu}_5\text{Zr}_8$  during the continuous heating of  $\text{Cu}_{50}\text{Zr}_{50}$  glass with a heating rate of 0.835 K/min (0.835 °C/min), this phase was not observed in the present work, which is consistent with the recent findings of Zhou and Napolitano.<sup>[22]</sup> These differing reports suggest that, although the presently reported devitrification sequence was observed consistently for heating rates from 10 K/min to 60 K/min (10 °C/min to 60 °C/min), much lower heating rates may result in a different phase selection response. Recently, Louzguine *et al.*<sup>[57]</sup> reported the primary formation of monoclinic martensitic type  $\text{CuZr}$  phase in  $\text{Cu}_{50}\text{Zr}_{50}$ . However, in this study, neither of the previously reported<sup>[40,48]</sup>  $\text{CuZr}$  martensitic transformation product phases (B2 → B19' + B33) were observed under the devitrification conditions examined here. In addition to heating rate effects, such differences in observed crystallization products may originate from small differences in trace impurity content.

## V. CONCLUSIONS

The DSC analysis of phase transitions using heating rates from 10 K/min to 60 K/min (10 °C/min to 60 °C/min) suggests that the reactions are essentially isokinetic over this range. Accordingly, it is expected that the phase sequences observed in the detailed *in situ* X-ray analysis will persist over this range, although relative growth and dissolution rates may vary. Moreover, our results demonstrate that the *in situ* HEXRD method is, in principle, well suited to deconvolve the multiple-phase diffraction patterns observed during devitrification. The temporal resolution remains as the main limitation

to direct observation of the primary crystallization event.

Supported by quantitative X-ray measurement of phase fractions, this analysis provides a thermodynamically self-consistent description of devitrification in a  $\text{Cu}_{50}\text{Zr}_{50}$  glass under constant-heating-rate (10 K/min [10 °C/min]). The sequence involves the formation of CuZr (B2),  $\text{Cu}_{10}\text{Zr}_7$ , and  $\text{CuZr}_2$  phases from the amorphous precursor at 706 K (433 °C), decomposition of B2 into more stable  $\text{Cu}_{10}\text{Zr}_7$  and  $\text{CuZr}_2$  upon heating to 789 K (516 °C), and reprecipitation of B2 upon heating above 1002 K (729 °C), accompanied by the dissolution of  $\text{Cu}_{10}\text{Zr}_7$  and  $\text{CuZr}_2$  until the transformation to B2 is complete at 1045 K (772 °C).

Although several details have been revealed quantitatively, three important questions remain. First, how can the discrepancy be reconciled between our results and the reported findings of Kneller *et al.*, in which the  $\text{Cu}_5\text{Zr}_8$  phase was observed in the devitrification sequence for this alloy (at the much lower heating rate of 0.835 K/min [0.835 °C/min])? This will require a more comprehensive investigation at low heating rates. Second, can the rapid multiphase crystallization event be resolved sufficiently to distinguish the individual contributing phenomena? Third, what are the relative influences of chemical partitioning, diffusion, strain, and defect accommodation in phase selection and the evolution of structure? These are topics of ongoing investigation.

## ACKNOWLEDGMENTS

This work was supported by the U.S. Department of Energy, Office of Basic Energy Science, Division of Materials Sciences and Engineering. The research was performed at the Ames Laboratory. Ames Laboratory is operated for the U.S. Department of Energy by Iowa State University under Contract No. DE-AC02-07CH11358. Synchrotron experiments were performed at the Advanced Photon Source, Argonne National Laboratory, under Grant No. DE-AC02-06CH11357. The authors also would like to thank Dr. Y. Eren Kalay, from Ames Laboratory, for assistance with TEM imaging.

## APPENDIX A

The modeled intensity,  $I^M(Q, \phi)$ , where  $Q$  is ( $Q = \frac{4\pi \sin \theta}{\lambda}$ ) for the general case can be written as follows:

$$I^M(\lambda, \theta, \phi) = L(\lambda, \theta) \times \sum_p A_p(\lambda) s_p P_p(\lambda) PV_p(\theta) m_p(\theta) [F_p(\theta)]^2 \quad [\text{A1}]$$

where the sum is taken over all phases ( $p$ ), and where  $L(\lambda, \theta)$  is the Lorentz polarization factor

$\left( L(\lambda, \theta) = \frac{P_h(\lambda) + (1 - P_h(\lambda)) \cos^2 2\theta}{2 \sin^2 \theta \cos \theta} \right)$ ,  $A_p(\lambda)$  is an absorption factor, which is not refined for constant wavelength data because the correction is indistinguishable from thermal motion effects,  $s_p$  is a phase fraction weighting factor,  $P_p(\lambda)$  is a preferred orientation factor,  $PV_p(\theta)$  is a pseudo-Voigt shape function (Type 2), which is a linear combination of Gaussian and Lorentzian functions,  $m_p(\theta)$  is a multiplicity factor,  $F_p(\theta)$  is the structure factor, and  $P_h(\lambda)$  is the polarization fraction. For the work described here, we use a constant wavelength and set  $P_h = 0.950$ . In addition, we take  $P_p$  and  $m_p$  as unity. Thus, for the case described here, the model becomes the following:

$$I(\theta) = L(\theta) \sum_p A_p s_p PV_p(\theta) |F_p(\theta)|^2 + I_b(\theta) \quad [\text{A2}]$$

where the optimization simply involves fitting the remaining three parameters,  $s_p$ ,  $PV_p(\theta)$ , and  $F_p(\theta)$ , where  $s_p$  is a scalar,

$$PV_p(\theta) = \eta L(\theta) + (1 - \eta) G(\theta) \quad [\text{A3}]$$

and

$$|F_p(\theta)|^2 = \left| \sum_p f_p(\theta) e^{2\pi i (k \cdot \vec{r}_n)} \right|^2 \quad [\text{A4}]$$

where  $\eta$  determines the weighting of Gaussian ( $G(\theta)$ ) and Lorentzian ( $L(\theta)$ ) components,<sup>[49]</sup>  $f_p$  is an atomic scattering factor,  $\vec{r}_n$  gives the atomic positions and the sum is taken over the unit cell. The background intensity,  $I_b(\theta)$  were modeled using a background profile function as follows:

$$I_b(\theta) = B_1 + \sum_{j=1}^N \left( B_{2j} \frac{(4\pi \sin \theta / \lambda)^{2j}}{j!} + B_{2j+1} \frac{j!}{(4\pi \sin \theta / \lambda)^{2j}} \right) \quad [\text{A5}]$$

where  $B_1$  is a constant,  $N$  is the number of coefficients, and the values of  $B_i$  are determined by least squares during Rietveld refinement process.

An example of profile fitting using Rietveld refinement is shown by the sequence in Figure 7 for three diffraction peaks corresponding to the CuZr (B2) structure with a space group of Pm-3m with atomic positions of Cu ( $\frac{1}{2}$ ,  $\frac{1}{2}$ ,  $\frac{1}{2}$ ) and Zr (0, 0, 0) at 1216 K (943 °C). The refinement is started from the raw data (Figure 7(a)) and done in proper order of applying Lorentz-polarization and background functions (Figure 7(b)), scale factor (Figure 7(c)), structure factor including lattice parameters (Figure 7(d)), Gaussian and Lorentzian peak profile functions (Figure 7(e)), and structure factor including thermal motion using isotropic thermal displacement parameters (Uiso) (Figure 7(f)).

Rietveld refinement provides an accurate determination of structural properties. After achieving a satisfactory profile fitting, the lattice parameter of B2 is found to change from 3.2810 Å (at room temperature) to 3.29616 Å when heated to 1216 K (943 °C). A specific



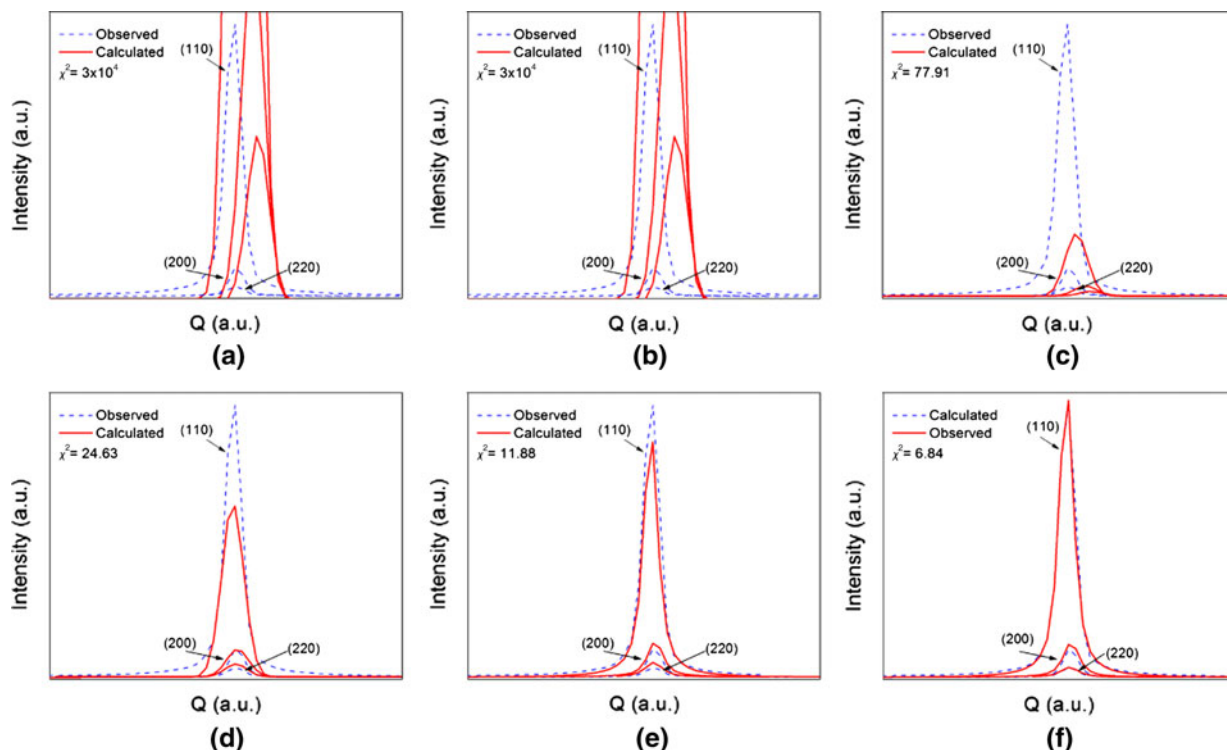


Fig. 7—An example of Rietveld refinement sequence of CuZr (B2) phase at 1216 K (943 °C) (a–f); starting with (a) raw data, and refining with (b) Lorentz-polarization factor and background function, (c) phase scalar factor, (d) structure factor including lattice parameters, (e) Gaussian and Lorentzian peak profile functions, and (f) isotropic thermal displacement parameters. The goodness of fit factors are given inset the figures.

benefit of the Rietveld analysis is that the refined model provides a quantitative phase analysis, in which the weight fraction  $w_i$  of each crystalline constituent phase can be determined from the corresponding phase scale parameter,  $s_i$  according to the following relationship:

$$w_i = \frac{s_i Mu_i}{\sum_j s_j Mu_j} \quad [A6]$$

where  $Mu_i$  is the unit cell mass. This analysis is based on the normalization condition  $\sum w_i = 1.0$ .

## REFERENCES

1. A. Inoue: *Acta Mater.*, 2001, vol. 49, pp. 2645–52.
2. W. Wang: *Mater. Sci. Eng., R*, 2004, vol. 44, pp. 45–89.
3. A. Inoue: *Acta Mater.*, 2000, vol. 48, pp. 279–306.
4. S. Shin: *Mater. Sci. Forum*, 2004, vols. 449–452, pp. 945–48.
5. J.R. Morris, M. Xu, Y.Y. Ye, D.J. Sordet, and M.J. Kramer: *Acta Mater.*, 2007, vol. 55, pp. 5901–09.
6. Y.E. Kalay, L.S. Chumbley, and I.E. Anderson: *J. Non-Cryst. Solids*, 2008, vol. 354, pp. 3040–48.
7. Y.E. Kalay, C. Yeager, L.S. Chumbley, M.J. Kramer, and I.E. Anderson: *J. Non-Cryst. Solids*, 2010, vol. 356, pp. 1416–24.
8. M. Calin, J. Eckert, and L. Schultz: *Scripta Mater.*, 2003, vol. 48, pp. 653–58.
9. U. Kuhn, J. Eckert, N. Mattern, and L. Schultz: *Appl. Phys. Lett.*, 2002, vol. 80, pp. 2478–80.
10. J. Eckert, J. Das, S. Pauly, and C. Duhamel: *Adv. Eng. Mater.*, 2007, vol. 9, pp. 443–53.
11. T. Abe, M. Shimono, M. Ode, and H. Onodera: *Acta Mater.*, 2006, vol. 54, pp. 909–15.
12. W. Yang, F. Liu, H. Liu, H.F. Wang, Z. Chen, and G.C. Yang: *J. Alloys Compd.*, 2009, vol. 484, pp. 702–07.
13. A.I. Zaitsev, N.E. Zaitseva, J.P. Alexeeva, S.F. Dunaev, and Y.S. Nechaev: *Phys. Chem. Chem. Phys.*, 2003, vol. 5, pp. 4185–96.
14. W.H. Wang: *Progr. Mater. Sci.*, 2007, vol. 52, pp. 540–96.
15. Y. Shen, E. Ma, and J. Xu: *J. Mater. Sci. Tech.*, 2008, vol. 24, pp. 149–52.
16. T. Fukami, H. Yamamoto, D. Okai, Y. Yokoyama, Y. Yamasaki, and A. Inoue: *Mater. Sci. Eng., B*, 2006, vol. 131, pp. 1–8.
17. E. Kneller: *Z. Metallkd.*, 1986, vol. 77, pp. 152–63.
18. K. Buschow: *J. Appl. Phys.*, 1981, vol. 52, pp. 3319–23.
19. Z. Altounian: *J. Appl. Phys.*, 1982, vol. 53, pp. 4755–60.
20. F. Jiang, D.H. Zhang, L.C. Zhang, Z.B. Zhang, L. He, J. Sun, and Z.F. Zhang: *Mater. Sci. Eng., A*, 2007, vol. 467, pp. 139–45.
21. J. Eckert, J. Das, S. Pauly, and C. Duhamel: *J. Mater. Res.*, 2007, vol. 22, pp. 443–53.
22. S.H. Zhou and R.E. Napolitano: *Acta Mater.*, 2010, vol. 58, pp. 2186–96.
23. Y. Calvayrac, J.P. Chevalier, M. Harmelin, A. Quivy, and J. Bigot: *Phil. Mag., B*, 1983, vol. 48, pp. 323–32.
24. G.V. Hillmann and W. Hofmann: *Z. Metallkd.*, 1965, vol. 56, pp. 279–86.
25. P. Forey, J.L. Glimois, and J.L. Feron: *J. Less-Common Met.*, 1986, vol. 124, pp. 21–27.
26. A.J. Perry and W. Hugi: *J. Inst. Met.*, 1972, vol. 100, pp. 378–80.
27. J. Glimois, P. Forey, and J.L. Feron: *J. Less-Common Met.*, 1985, vol. 113, pp. 213–24.
28. D. Arias and J.P. Abriata: *Bull. Alloy Phase Diagr.*, 1990, vol. 11, pp. 452–59.
29. L. Bsenko: *J. Less-Common Met.*, 1975, vol. 40, pp. 365–66.
30. J. Gabathuler, P. White, and E. Parthe: *Acta Crystallogr., B*, 1975, vol. 31, pp. 608–10.
31. F. Eshelman and J.F. Smith: *Acta Crystallogr., B*, 1972, vol. 28, pp. 1594–1600.
32. C. Becle, B. Bourniquel, G. Develey, and M. Saillard: *J. Less-Common Met.*, 1979, vol. 66, pp. 59–66.

33. L. Bsenko: *Acta Crystallogr., B*, 1976, vol. 32, pp. 2220–24.
34. J.M.C.B. Oliveira and I.R. Harris: *J. Mater. Sci.*, 1983, vol. 18, pp. 3649–60.
35. E. Kneller, Y. Khan, and U. Gorres: *Z. Metallkd.*, 1986, vol. 77, pp. 43–48.
36. J.M. Joubert, R. Cerny, K. Yvon, M. Latroche, and A. PercheronGuegan: *Acta Crystallogr., C*, 1997, vol. 53, pp. 1536–38.
37. M. Kirkpatrick, J.F. Smith, and W.L. Larsen: *Acta Crystallogr., A*, 1962, vol. 15, pp. 894–903.
38. J.L. Glimois, C. Beche, G. Develey, and J.M. Moreau: *J. Less-Common Met.*, 1979, vol. 64, pp. 87–90.
39. E.M. Carvalho and I.R. Harris: *J. Mater. Sci.*, 1980, vol. 15, pp. 1224–30.
40. D. Schryvers: *Scripta Mater.*, 1997, vol. 36, pp. 1119–25.
41. M. Kirkpatrick, D.M. Bailey, and J.F. Smith: *Acta Crystallogr., A*, 1962, vol. 15, pp. 252–55.
42. G. Ghosh: *Acta Mater.*, 2007, vol. 55, pp. 3347–74.
43. J.W. Visser: *Acta Crystallogr., B*, 1977, vol. 33, p. 316.
44. J.K. Brandon, R.Y. Brizard, P.C. Chieh, R.K. McMillan, and W.B. Pearson: *Acta Crystallogr., B*, 1974, vol. 30, pp. 1412–17.
45. M. Nevitt and J.W. Downey: *Trans. TMS-AIME*, 1962, vol. 224, pp. 195–96.
46. R.L. Freed and J.B. Vander Sande: *J. Non-Cryst. Solids*, 1978, vol. 27, pp. 9–28.
47. H. Okamoto: *J. Phase Equilib. Diffus.*, 2008, vol. 29, p. 204.
48. S.H. Zhou and R.E. Napolitano: *Scripta Mater.*, 2008, vol. 59, pp. 1143–46.
49. A.C. Larson and R.B. Von Dreele: *LAUR*, 2004, pp. 86–748.
50. B.H. Toby: *J. Appl. Crystallogr.*, 2001, vol. 34, pp. 210–13.
51. R.E. Napolitano and H. Meco: *Metall. Mater. Trans. A*, 2004, vol. 35A, pp. 1539–53.
52. M.J. Kramer, H. Mecco, K.W. Dennis, E. Vargonova, R.W. McCallum, and R.E. Napolitano: *J. Non-Cryst. Solids*, 2007, vol. 353, pp. 3633–39.
53. H. Kissinger: *Anal. Chem.*, 1957, vol. 29, pp. 1702–06.
54. H.J. Eifert, B. Elschner, and K.H.J. Buschow: *Phys. Rev. B*, 1982, vol. 25, pp. 7441–48.
55. M. Kasai, J. Saida, M. Matsushita, T. Osuna, E. Matsubara, and A. Inoue: *J. Phys.: Condens. Matter.*, 2002, vol. 14, pp. 13867–77.
56. D.V. Louzguine-Luzgin, A.R. Yavari, and A. Inoue: *Appl. Phys. Lett.*, 2005, vol. 86, pp. 1–3.
57. D.V. Louzguine-Luzgin, G. Xie, Q. Zhang, C. Suryanarayana, and A. Inoue: *Metall. Mater. Trans. A*, 2010, vol. 41A, pp. 1664–69.